

Analysis, Design, and Optimization of Spiral Inductors and Transformers for Si RF IC's

Ali M. Niknejad, *Student Member, IEEE*, and Robert G. Meyer, *Fellow, IEEE*

Abstract—Silicon integrated circuit spiral inductors and transformers are analyzed using electromagnetic analysis. With appropriate approximations, the calculations are reduced to electrostatic and magnetostatic calculations. The important effects of substrate loss are included in the analysis. Classic circuit analysis and network analysis techniques are used to derive two-port parameters from the circuits. From two-port measurements, low-order, frequency-independent lumped circuits are used to model the physical behavior over a broad-frequency range. The analysis is applied to traditional square and polygon inductors and transformer structures as well as to multilayer metal structures and coupled inductors. A custom computer-aided-design tool called ASITIC is described, which is used for the analysis, design, and optimization of these structures. Measurements taken over a frequency range from 100 MHz to 5 GHz show good agreement with theory.

Index Terms—Monolithic inductors and transformers, optimization of Si inductors and transformers, spiral inductors and transformers.

I. INTRODUCTION

SILICON integrated circuits (IC's) are finding wide application in the gigahertz frequency range. Modern bipolar (Bi), complementary metal-oxide-semiconductor (CMOS), and BiCMOS processes provide high f_T transistors, allowing Si radio-frequency (RF) IC's to compete with GaAs IC's in the important low-gigahertz frequency ranges. However, the lossy Si substrate makes the design of high Q reactive components difficult. Despite this difficulty, the low cost of Si IC fabrication over GaAs IC fabrication and the potential for integration with baseband circuits makes Si the process of choice in many RF IC applications.

The demands placed on portable wireless communication equipment include low cost, low supply voltage, low power dissipation, low noise, high frequency of operation, and low distortion. These design requirements cannot be met satisfactorily in many cases without the use of RF inductors. Hence, there is a great incentive to design, optimize, and model spiral inductors fabricated on Si substrates. This topic is addressed in this paper.

Since the introduction of Si spiral inductors [1], many authors have reported higher performance inductors on Si substrates, primarily utilizing advances in processing technology. This has included higher conductivity metal layers to reduce

the loss resistance of the inductor [2], use of multimetal layers to increase the effective thickness of the spiral inductor and thereby reduce loss, the connection of multimetal layer spirals in series to reduce the area of the inductors [3], [4], low-loss substrates to reduce losses in the substrate at high frequency [5], and thick oxide or floating inductors to isolate the inductor from the lossy substrate [6]. Little, though, has been written on the analysis and optimization of these structures.

In [7], an analysis approach is presented where an equivalent circuit for each segment of the spiral is calculated and the inductor is considered as an interconnection of such segments. The approach is limited, though, as many important effects are not included. For instance, nonuniform current distribution due to skin and proximity effects within each segment is not considered. In addition, the impedance to substrate is calculated using a two-dimensional approach, making it difficult to apply to arbitrary structures or to coupled inductors.

Most past researchers have used measurement results on previously built inductors to construct models. While this technique is most practical, it does not allow the possibility of optimization, nor does it allow the circuit designer freedom to choose parameters such as inductance, resistance, capacitance, and Q . Alternatively, researchers have used commercial three-dimensional electromagnetic simulators [8], [9] to design and analyze inductors and transformers. While this approach is accurate, it can be computationally very expensive and time consuming. This prevents the designer from performing optimization. In this paper, we present an accurate and computationally efficient approach to overcome some of these difficulties.

II. EQUIVALENT CIRCUIT FORMULATION

A. Electromagnetic Formulation

Consider a typical spiral inductor or transformer. It consists of series and parallel interconnection of metal segments. Applying Maxwell's equations to the conductive portions of such a structure, we obtain [10]

$$\int E_0 \cdot dl - \int \frac{J}{\sigma} \cdot dl - \int \frac{\partial A}{\partial t} \cdot dl - \int \nabla \phi \cdot dl = 0 \quad (1)$$

where E_0 is the applied field, J is the current density, σ is the conductivity of the metal segment, A is the magnetic vector potential, and ϕ is the electric scalar potential. The first term of the above equation arises from the applied field, the second term represents the internal impedance of the segments, the

Manuscript received May 27, 1997; revised November 17, 1997. This work was supported by the U.S. Army Research Office under Grant DAAH04-93-G-0200.

The authors are with the Department of Electrical Engineering and Computer Science, University of California, Berkeley, CA 94720-1772 USA.

Publisher Item Identifier S 0018-9200(98)06998-4.

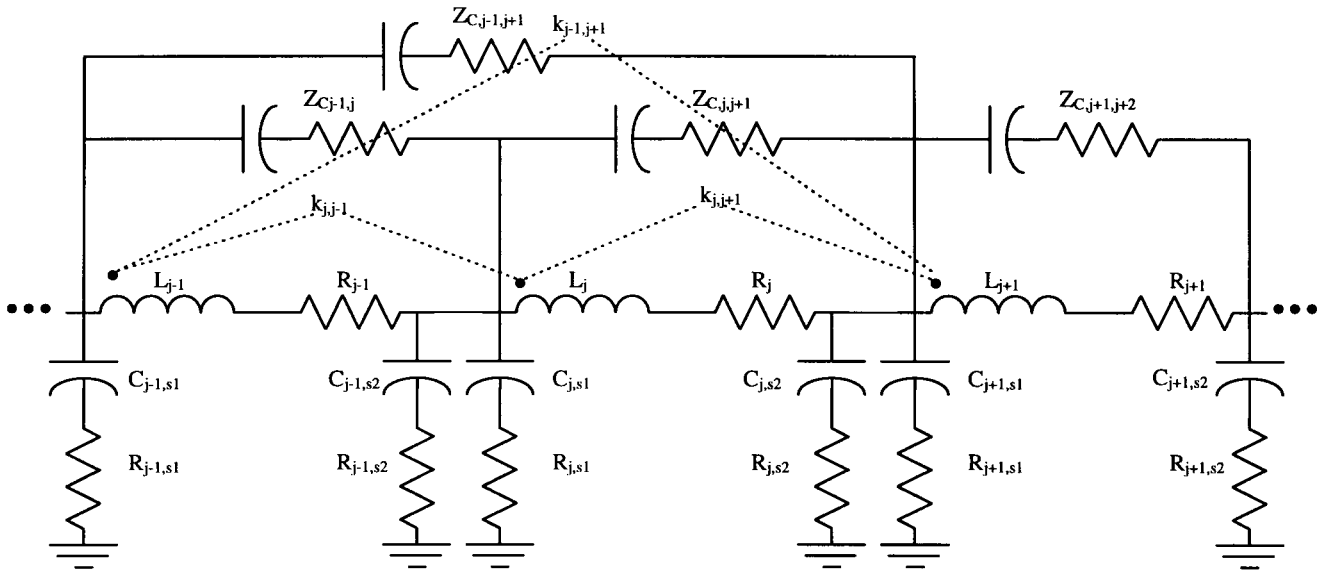


Fig. 1. Equivalent circuit model of spiral segments.

third term represents external inductance, and the fourth term is the capacitive term.

The magnetic and electric potentials are integrals over the charges and currents in the circuit. In the time-periodic case, we have

$$\phi(x, y, z) = \int_v \frac{\rho(x', y', z') e^{-jkR}}{4\pi\epsilon R} dV' \quad (2)$$

$$A(x, y, z) = \mu \int_v \frac{J(x', y', z') e^{jkR}}{4\pi R} dV'. \quad (3)$$

The above retarded potentials can be simplified to static potentials since at frequencies of interest, the exponential term is nearly unity. As they stand, though, the above equations are impractical since they involve integrating over all charges and currents, including those that flow through the substrate. If, however, we replace the R^{-1} term involving the free-space Green function with the appropriate Green functions over a multilayer substrate, the volume of integration reduces to metal segments containing the charge and currents. In [11], we derive the electrostatic Green function over a multilayer conductive substrate that can be used in (2).¹

By expanding A and ϕ in (1) using (2) and (3) and by considering the currents and charges in each segment separately, we obtain a system of linear equations [12]. Each equation has terms representing the internal impedance of each segment, as well as the mutual magnetic and electrical coupling between each segment and every other segment, and finally terms representing the magnetic and electric coupling to the substrate.

B. Circuit Equation Formulation

From a circuit point of view, (1) can be interpreted as shown in Fig. 1. To derive the two-port parameters of such a structure, we must solve the circuit equations by selecting

¹The magnetostatic Green function can be derived in an analogous way. The computation of the inductance matrix over a lossy conductive substrate is the subject of another paper.

an appropriate number of independent equations, using, for instance, nodal or loop analysis. Let us consider the topology of the network in relation to the spiral. For a typical p -sided spiral of n turns, there are $s = n \times p$ segments. Each segment has one branch associated with the series inductance and resistance and one branch associated with the substrate impedance. Assuming a dense capacitive coupling impedance matrix, this adds an additional $s(s-1)/2$ branches of lossy capacitors from segment to segment. Hence, the total number of branches $B = (s+1)(s+2)/2$. The total number of nodes N in the circuit is simply one plus the number of segments, or $s+1$. Consequently, the total number of fundamental loops L in the circuit equals $L = B - N \sim O(s^2)$.

Although loop equations are a more natural formulation, due to the mutual inductive nature of the circuit, the number of required equations is one order of magnitude larger than the number of node equations. Hence, nodal analysis is the method of choice. Writing the nodal equations at node j results in

$$\frac{V_j}{Z_{j0}^C} + \sum_{k \neq j} \frac{V_j}{Z_{jk}^C} - \sum_{k \neq j} \frac{V_k}{Z_{jk}^C} + I_j - I_{j-1} = 0. \quad (4)$$

In the above equation, V_j is the voltage at node j , I_j is the current flowing into segment j , and Z_{jk}^C is the lossy capacitive impedance coupling segment j and k . The above equations involve the voltages and currents in the segments, similar to modified nodal analysis. The voltage across each segment is related to the currents flowing in the segments by

$$V_j - V_{j+1} = \sum_k Z_{jk}^L I_k \quad (5)$$

where Z_{jk}^L is an entry of the symmetric inductance matrix Z^L . The diagonal terms represent the internal impedance of each segment, whereas the off-diagonal terms represent the magnetic coupling between segments. The above system of equations yields an invertible complex frequency-dependent matrix. Since there are $2s$ equations in (4) and (5), the system can be solved directly using Gaussian elimination with

pivoting or LU factorization, in time $O((2s)^3)$. However, the matrix naturally partitions into four square matrices as

$$\begin{bmatrix} Y^C & D^T \\ D & -Z^L \end{bmatrix} \begin{bmatrix} V \\ I \end{bmatrix} = \begin{bmatrix} I_s \\ V_s \end{bmatrix}. \quad (6)$$

Y^C is a matrix with elements

$$[Y_{ij}^C] = \frac{-1}{Z_{ij}^C} \quad [Y_{ii}^C] = \sum_k \frac{1}{Z_{ik}^C}. \quad (7)$$

D is an upper triangular band matrix with its diagonal entries as 1 and with superdiagonal entries as -1 . Rewriting (6), we have

$$(Y^C + D^T Y^L D)V = I_s + D^T Y^L V_s \quad (8)$$

$$I = Y^L(DV - V_s) \quad (9)$$

where $Y^L = (Z^L)^{-1}$ is the inverse of the inductance matrix. As we will see later, Y^L is known *a priori*, and no explicit matrix inversion needs to be performed. In addition, due to the simple structure of D , the matrix products involving D and its transpose can be done in order $O(s^2)$. Hence, in forming (8) and (9), no explicit matrix products need to be formed. Thus, we can solve (8) by using an LU decomposition of $(Y^C + D^T Y^L D)$ and then solve (9) directly for I . Therefore, the solution of (6) is dominated by one LU decomposition of an $s \times s$ matrix, which can be performed in time $O(s^3)$. This is more than eight times faster than solving (6) directly.

C. Inductance Matrix

The inductance matrix Z^L must be computed to solve (6). At low frequency, this matrix may be computed easily since the self- and mutual inductance of each segment can be approximated in closed form by using the geometric mean distance (GMD) approximation. Grover [13] provides formulas for such calculations for fairly arbitrary configurations. In [14], an explicit formula appears for the GMD between two finite thickness parallel rectangular cross sections. In a square spiral, all segments are parallel and these formulas suffice. However, for polygon spirals or for arbitrary structures, we need the mutual inductance between nonparallel segments situated in general in three-dimensional space. While the exact formula for filaments placed in these configurations is known in closed form, the GMD concept is difficult to generalize in these cases, as the integrals are not easily evaluated. In addition, at high frequency, these approximations fail altogether as the current distributions become nonuniform and the GMD approximation fails.

The nonuniformity in the current distribution is due not only to the skin effect but also to proximity effects of neighboring current segments. Hence, although many past authors [7] have analyzed and developed closed-form equations for current constriction in an isolated conductor, these results are not directly applicable to the spiral inductor due to proximity effects.

In [14], a nice technique is developed to handle this problem without abandoning the closed-form equations available. The current distribution in the conductor can be approximated in a step-wise fashion by breaking up each segment into

subsegments of uniform current distribution. Although this technique is general and accurate, it is computationally expensive. Consider a typical ten-sided spiral with ten turns as an example. Such a spiral has 100 segments, and if we were to divide each segment further into five parallel segments, this would involve 500 segments and a corresponding 500×500 matrix inversion. To alleviate the demand on computational resources, we will assume that the segment current distribution is only influenced by a small set of neighboring segments. For a typical planar spiral, this might involve only two neighboring segments.

We rederive the results presented in [14] with this approximation in mind. For a set of N segments, let the (i, j) segment represent the j th subsegment of segment i and let N_i denote the number of such subsegments in segment i . Let I_{ij} be the current in the (i, j) segment and let I_i be the total current in segment i . With this notation, the voltage across the (i, j) segment is given by

$$V_{ij} = \sum_{k=0}^N \sum_{m=1}^{N_k} (r_{ij} \delta_{ki} \delta_{jm} + j\omega L_{ij,km}) I_{km}. \quad (10)$$

In the above equation, r_{ij} is the resistance of the (i, j) conductor, δ_{ij} is the Kroniker delta function, and $L_{ij,km}$ is the mutual inductance between subsegments (i, j) and (k, m) . Let C_i denote the set of segments in the neighborhood of segment i , or the set of segments that influence the current distribution of segment i [15]. Equation (10) may be broken up as follows:

$$V_{ij} = V_{ij}^L + V_{ij}^G = \sum_{k \in C_i} \sum_{m=1}^{N_k} Z_{ij,km} I_{km} + \sum_{k \notin C_i} j\omega L_{ik} I_k. \quad (11)$$

Inverting the first term corresponding to the local voltage at segment (i, j) , we obtain

$$I_{ij} = \sum_{k \in C_i} \sum_{m=1}^{N_k} Y_{ij,km} V_{km}^L. \quad (12)$$

The total current in segment i is given by

$$I_i = \sum_{j=1}^{N_i} I_{ij} = \sum_{k \in C_i} \sum_{j=1}^{N_i} \sum_{m=1}^{N_k} Y_{ij,km} V_{km}^L. \quad (13)$$

If we make the reasonable assumption that the voltage across each subsegment (i, j) is independent of the index j (as was done in [14]), then (13) becomes

$$I_i = \sum_{k \in C_i} V_{km}^L \sum_{j=1}^{N_i} \sum_{m=1}^{N_k} Y_{ij,km} = \sum_{k \in C_i} V_{km}^L Y_{ik}^L. \quad (14)$$

Equation (11) may be rewritten as

$$V_i = \sum_{k \in C_i} Z_{ik}^L I_k + \sum_{k \notin C_i} j\omega L_{ik} I_k. \quad (15)$$

Repeating for all i , one generates the desired matrix equation. The above technique involves one matrix inversion going from (11) to (12) and another matrix inversion of reduced order going from (14) to (15). The latter matrix inversion can be neglected since the matrix is small. Assuming

that matrix inversion is the most computationally intensive operation—and that it is done $O(s^3)$, whereas the original technique presented in [14] is $O[(s \times r)^3]$, where s is the total number of segments and r is the average number of subsegments—this technique is $O[s \times (q \times r)^3]$, where q is one plus the average number of neighbors for each segment. Hence, this technique is s^2/q^3 faster and demands s^2/q^2 less memory to store the matrix. For the example given earlier, a ten-sided, ten-turn spiral with two neighbors and five subsegments per segment, this means that this technique is 370 times faster and more than 1000 times less memory intensive.

D. Capacitance Matrix

Techniques for the calculation of the capacitance matrix are well developed and have wide applications. However, most approaches consider the capacitance matrix of conductors in free space, or over an ideal ground plane. In [11], we present an efficient technique that is directly applicable to the case of a conductive substrate.

With this approach, the true three-dimensional capacitance matrix of the device segments can be extracted and used in (6). Various effects can be included in the capacitance matrix calculation, such as the presence of substrate taps and substrate shields [16]. The important effect of substrate coupling between structures residing on the same substrate can also be included. For more details, refer to [11].

III. ASITIC: A COMPUTER-AIDED-DESIGN TOOL FOR INDUCTOR/TRANSFORMER DESIGN, ANALYSIS, AND OPTIMIZATION

Much is known about the optimization of the technological parameters of a process for optimal inductor performance [7]. Thicker or higher conductivity metal improves the quality factor Q at low frequencies, whereas a higher resistivity substrate and thicker oxide help to isolate the device from the substrate at high frequencies. The optimization of the geometry of inductors and transformers, though, is more difficult. Even for simple structures, such as square spirals, there are several parameters to optimize, including the area of the spiral, the metal width and spacing, and the number of turns. Not much can be said in general since the optimal geometry depends on the frequency of operation.

For instance, at low frequency, one usually uses the minimum spacing available to maximize magnetic coupling, but at high frequency, proximity effects and magnetic coupling favor a larger value of spacing [8]. This is illustrated in Fig. 2, where we plot the resistance of a typical spiral using two values of spacing. Similar considerations apply to the area of the spiral and the number of turns. At lower frequencies, large areas allow wider metal widths to meet a given inductance at lower values of series resistance and therefore higher Q . But at high frequencies, the Q is dominated by the substrate and smaller areas are favorable. This is doubly true for highly conductive substrates that suffer from eddy-current losses at high frequency [8].

With the introduction of multimetal structures, such as shunt and series connected spirals, the situation is even more

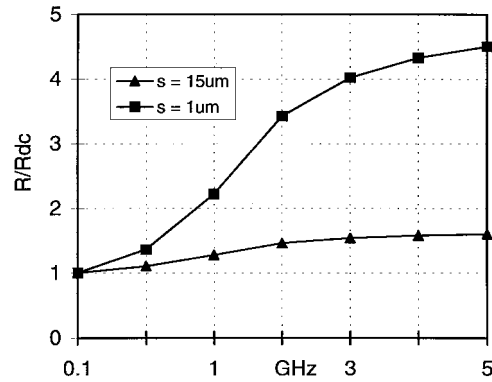


Fig. 2. Normalized spiral resistance as a function of frequency.

TABLE I
APPROXIMATE PROCESS PARAMETERS

Metal 2	$R_{sh} = 33\text{m}\Omega/\text{sq}$	$t = 1.27\mu\text{m}$	$C_{sub} = 14\text{aF}/\mu\text{m}^2$
Metal 1	$R_{sh} = 50\text{m}\Omega/\text{sq}$	$t = 1.00\mu\text{m}$	$C_{sub} = 21\text{aF}/\mu\text{m}^2$
Metal 0	$R_{sh} = 100\text{m}\Omega/\text{sq}$	$t = 0.40\mu\text{m}$	$C_{sub} = 105\text{aF}/\mu\text{m}^2$
Buried Layer	$\rho = 0.085\Omega\text{-cm}$	$t = 1\mu\text{m}$	p ⁺ Si
Bulk Substrate	$\rho = 20\Omega\text{-cm}$	$t = 675\mu\text{m}$	p ⁻ Si

complicated. Thus, the optimization of such structures must be done carefully on a case-by-case basis. To aid this process, a custom tool has been developed. The techniques presented in this paper have been collected into Analysis and Simulation of Inductors and Transformers for IC's (ASITIC),² a user-friendly computer-aided-design (CAD) tool designed to aid the RF circuit designer in the designing, optimizing, and modeling of the spiral inductor and transformers. The tool is flexible, allowing the user to trade off between speed and accuracy. For example, ASITIC can be used to quickly search the parameters space of an inductor optimization problem.

By working with the entire metal layout of the circuit at hand, ASITIC allows general magnetic and substrate coupling to be analyzed between different parts of the circuit. Parasitic metal extraction may also be performed, including the effects of the substrate, and the resulting SPICE file may be included in more accurate simulations. The final design of a spiral may be exported for final layout; this feature is convenient in the layout of complex geometry spirals (nonsquare spirals), since their hand layout is time consuming, especially when changes are made to the geometry of the spiral.

IV. MEASUREMENT RESULTS

A. Description of Process/Masurement Setup

All spiral inductors were fabricated in Philips Semiconductors' Qubic2 BiCMOS process. Approximate process parameters are given in Table I. Using on-chip cascade probes, the average two-port s-parameters of the spirals are measured from 100 MHz to 5 GHz. Since the measurement setup holds wafers in place using vacuum suction, the back plane of the substrate is effectively floating. The substrate surface is grounded by placing substrate taps near the spirals.

² See <http://www.eecs.berkeley.edu/~niknejad>.

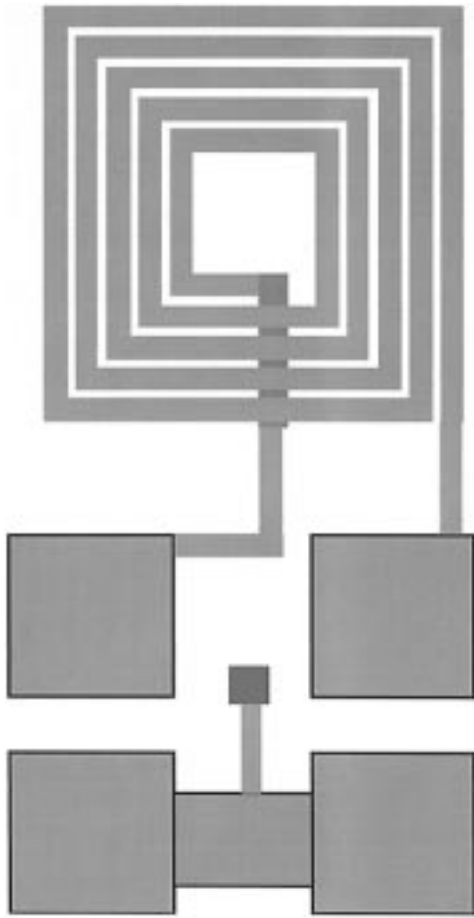


Fig. 3. Layout of spiral and probe pads for measurement.

Pad capacitance is deembedded by subtracting out the open-circuit structure y -parameters from the spiral y -parameters. The calibration procedure we use is the standard approach and is reported widely. But there is an intrinsic problem with this calibration approach that can render the measurement results inaccurate. Fig. 3 shows the layout of a typical spiral setup for measurement. To deembed the large substrate capacitance and resistance of the pad structure, the open-pad two-port parameters are also measured, as shown in Fig. 4. In the same figures, we show a schematic of the pad parasitics along with the spiral equivalent circuit. Clearly, the open-circuit pad structure does not contain the parasitic coupling between the spiral structure and the pads. In addition, the pad-to-pad coupling is different in the two cases shown, since the spiral itself tends to shield the pads from one another. Hence, the pad parasitics are not correctly deembedded from the measurement results.

To show this effect, we simulate a sample inductor with and without pads. Next, we deembed the pad parasitics from the simulation results with pads (just as one would in measurement), and the resulting extracted series inductance, resistance, and Q factor are shown in Fig. 5(a) and (b). The inductance value is in error but in both cases increases with frequency; the series resistance values, though, deviate dramatically as a function of frequency. Notice, too, that the trend comes out incorrect, increasing as a function of frequency instead

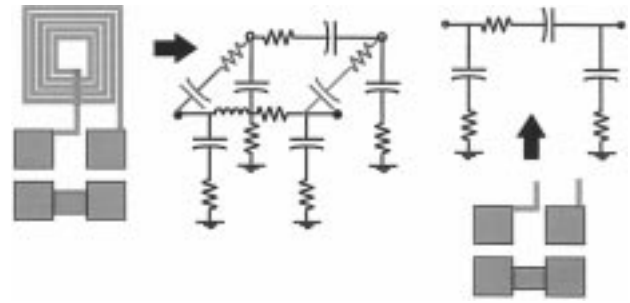


Fig. 4. Layout and equivalent circuit models of spiral and pads used for calibration procedure.

of decreasing. Also shown is the resulting error in the Q factor. In addition, this error can change the location of the peak Q -factor, resulting in suboptimal designs. Not shown are the equivalent extracted substrate impedance values. The measurement errors can produce dramatic differences here too, changing the substrate resistance by a factor of two. The substrate capacitance can actually change sign due to resonance phenomena. In the following sections, in order to match simulation results to measurements, we simulated our structures under the same conditions as they were measured.

To solve these problems, we can of course always minimize the parasitic coupling between the device under test and the pads by physically moving the structure away from the pads and by placing isolating substrate taps between the structures. Nevertheless, this requires large areas to be consumed on the chip. While this calibration problem occurs for a BiCMOS substrate, simulation also indicates some problems on an epitaxial CMOS substrate. The magnitude of the error, though, is much smaller. For instance, the series L and R change much less, and only the substrate impedance changes drastically due to the calibration step.

B. Extraction of Circuit Parameters from Measurement Data

At each frequency of interest, the equivalent pi-circuit of Fig. 6(a) can be extracted from y -parameters. By taking real and imaginary parts of Y_{12} , equivalent inductance and resistance are extracted. Similarly, input and output shunt capacitance and resistance to substrate may be extracted by taking real and imaginary parts of $Y_{11} + Y_{12}$ and $Y_{22} + Y_{12}$. Since the circuit is passive, it is also reciprocal, so that $Y_{12} = Y_{21}$. This extraction procedure is widely used and is simple to implement since the electrical parameters of the spiral are uniquely determined at each frequency. The drawback, though, is that the extracted inductance is not physical and contains the effects of the capacitive coupling, which tends to boost the inductance as a function of frequency, similar to a parallel tank. The extraction technique presented in [17] is superior in this regard.

In this paper, we use the standard extraction procedure to compare our simulation results to measurements. However, for our final device models, we use frequency-independent circuits such as shown in Fig. 6(b), which contain parasitic elements so that our extraction of inductance is more physical. On the other hand, there is no unique way to assign the parameters

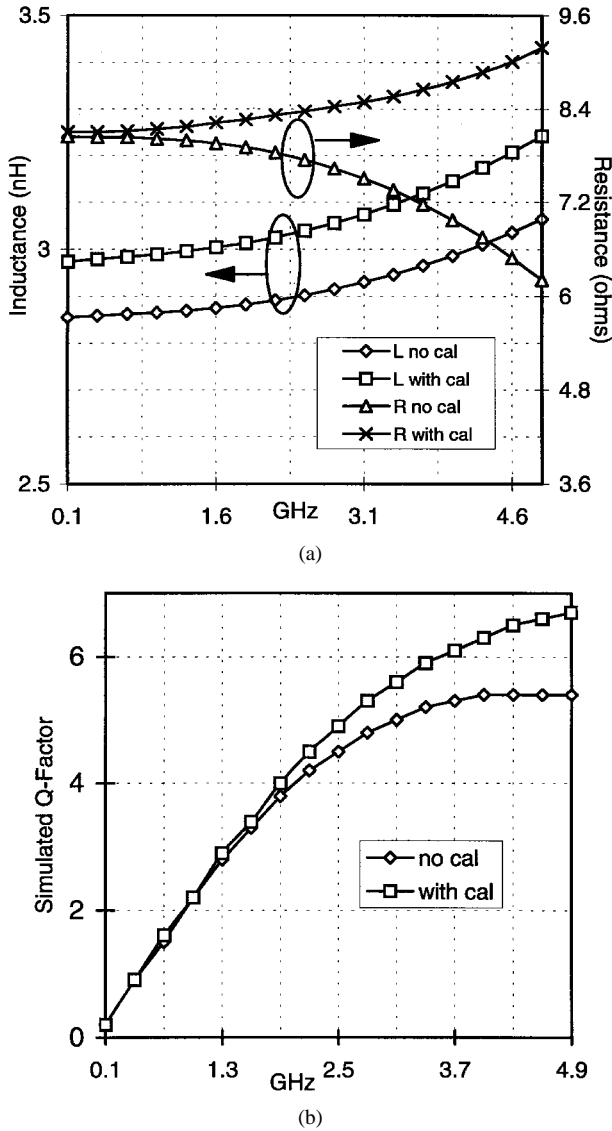


Fig. 5. (a) Extracted inductance and resistance of spiral inductor with and without calibration procedure. (b) Extracted quality factor Q with and without calibration procedure.

values of our models since we use optimization to fit a low-order frequency-independent model to a distributed structure over a broad frequency range.

The traditional approach of Q extraction involves computing

$$Q_1 = \frac{-\text{Im}(Y_{11})}{\text{Re}(Y_{11})}. \quad (16)$$

The above definition has the awkward property that the Q is zero at self-resonance. Since inductors are usually operated far from self-resonance, this does not present too many problems. But in some applications, the inductor is used as a resonant tank close to self-resonance. In such cases, it is more appropriate to define the Q using a 3-dB bandwidth definition

$$Q = \frac{\omega_0}{\Delta\omega_{3\text{dB}}}. \quad (17)$$

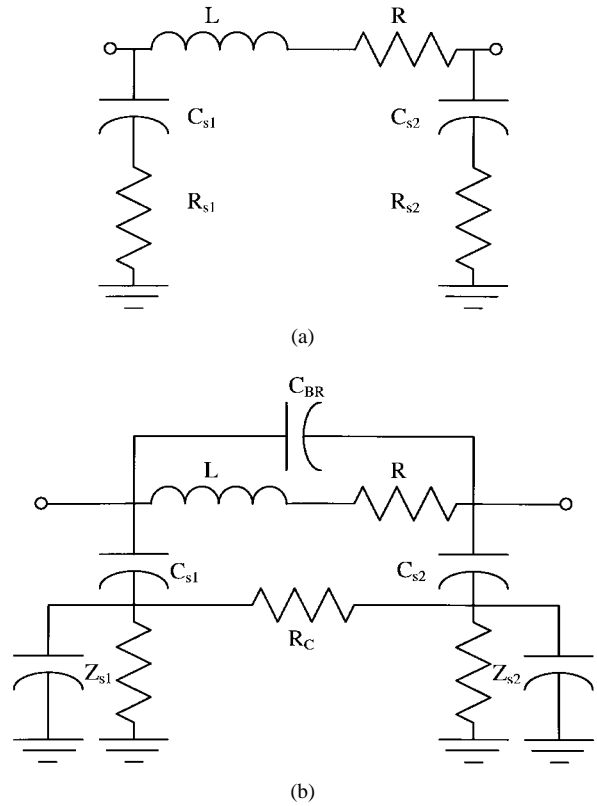


Fig. 6. (a) Traditional spiral inductor model. (b) Modified spiral inductor model.

Equally applicable, one may use the rate of change of phase at resonance

$$Q = \frac{\omega_0}{2} \left. \frac{d\phi}{d\omega} \right|_{\omega_0}. \quad (18)$$

The above equations are derived using second-order resonant circuits. For higher order circuits, perhaps the most general definition is based on ratio of energy stored in the circuit to energy dissipated per cycle, or

$$Q = \frac{W_{\text{stored}}}{W_{\text{diss}}} \Big|_{\text{per cycle}}. \quad (19)$$

The best approach to defining Q should be application dependent. Our approach to Q extraction is based on (18).

At each frequency of interest, an ideal capacitor is inserted in shunt with the inductor with admittance equal to the imaginary part of Y_{11} . The resulting admittance becomes

$$Y'(\omega) = j\omega C + Y_{11} \\ C = -\frac{\text{Im}[Y_{11}(\omega_0)]}{\omega_0}. \quad (20)$$

This capacitance will resonate the device at the frequency of interest ω_0 . By examining the rate of change of phase, one can find the equivalent Q

$$\left. \frac{d\phi}{d\omega} \right|_{\omega_0} = \frac{2Q}{\omega_0} = \frac{\angle Y'(\omega_0 + \delta\omega) - \angle Y'(\omega_0 - \delta\omega)}{2\delta\omega}. \quad (21)$$

To illustrate this approach, in Fig. 7 we plot the Q of a typical spiral inductor (square spiral with nine turns of

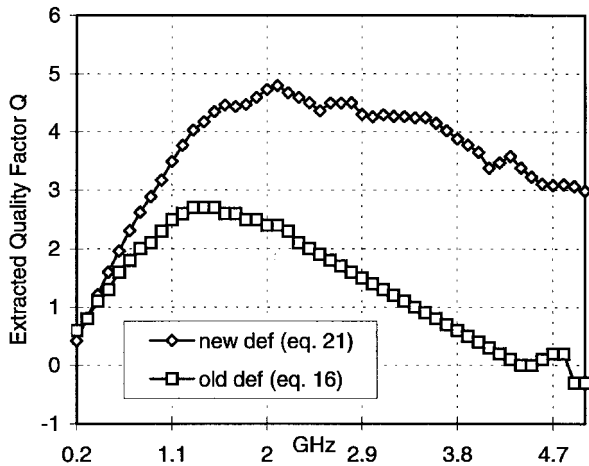


Fig. 7. Extracted quality factor Q of a nine-turn spiral by using (16) and (21).

dimensions given in the next section) using the definition present in (21). In the same plot, we show the traditional definition of Q , using (16). As we approach self-resonance, the two definitions deviate greatly. Notice also that the peak value of Q occurs at different frequencies for the two definitions.

In the following sections on measurement results, the data are measured at room temperature. It is important to calculate Q at the frequency and temperature of interest [18]. At low frequencies, the Q temperature coefficient (TC) will depend on the metal TC, whereas at high frequency, the Q will change due to the TC of the substrate resistance.

C. Square Spiral Inductors

Since square spirals are the most common inductors in Si RF IC's, we begin by comparing our simulation results of the previous section with measurement results. Many square spirals were fabricated, and measurement results were compared to simulation. The spirals have the following geometry: constant inner area $A_i = 44 \mu\text{m}$, constant width $w = 7 \mu\text{m}$, and constant spacing $s = 5 \mu\text{m}$, with turns $n = 5-10$. A chip layout of the eight-turn spiral appears in Fig. 8. For example, Fig. 9 shows the measured and simulated s -parameters for the eight-turn spiral. As can be seen from the figure, simulation s -parameters match the measured s -parameters well.

Fig. 10(a) plots the extracted series inductance from both measurement data and simulation data for the five- and eight-turn spirals. Good agreement is found for all spirals. For all spirals, the inductance is an increasing function of frequency. In reality, the physical inductance decreases as a function of frequency due to the current crowding at the edges of the conductors, which leads to a decrease in internal inductance.³ The extracted increase in L is due primarily to the coupling capacitance, which boosts the effective L as a function of frequency. For the smaller spirals, the same coupling capacitance tends to increase R as well, but the effect of the shunt substrate resistance is to lower the effective series R . For large

³For a highly conductive substrate, the eddy currents generated in the bulk substrate also lead to a decrease in inductance as a function of frequency, as these currents partially cancel the magnetic field generated by the device.

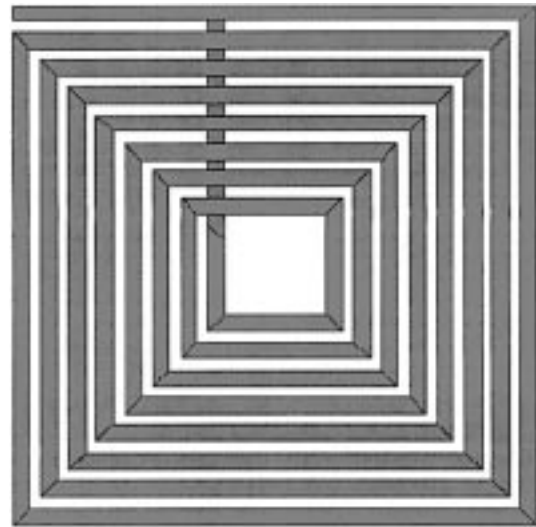


Fig. 8. Layout of eight-turn square spiral.

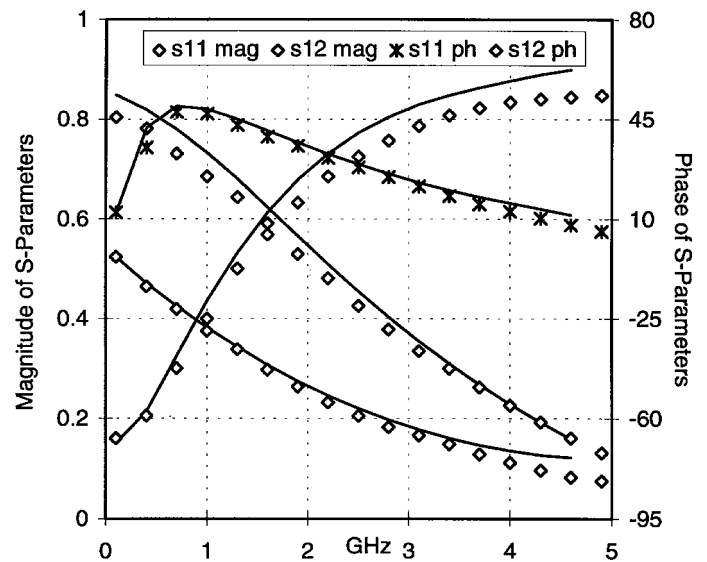


Fig. 9. Measured and simulated s -parameters of the eight-turn square spiral.

spirals in which substrate injection occurs at a lower frequency, the behavior of R is a decreasing function of frequency. For smaller spirals, the substrate injection is minimal due to a small substrate capacitance, and the effect of the coupling capacitance boosts R as a function of frequency.

Fig. 10(b) shows the Q -factor for the five- and eight-turn spirals. Here, we used the phase definition of (21) to compute Q . Good agreement is found between measurements and simulations. For the smaller five-turn spiral, the Q is an almost linear function of frequency, demonstrating that the substrate has negligible effects on the spiral, and the Q is approximately given by ωLR^{-1} . The larger eight-turn spiral, though, shows more complicated behavior due to the substrate. At low frequencies when the substrate impedance is large, simple linear behavior is observed. At high frequencies, when the substrate impedance is smaller than the inductive/resistive impedance of the spiral, the substrate loss dominates and the Q

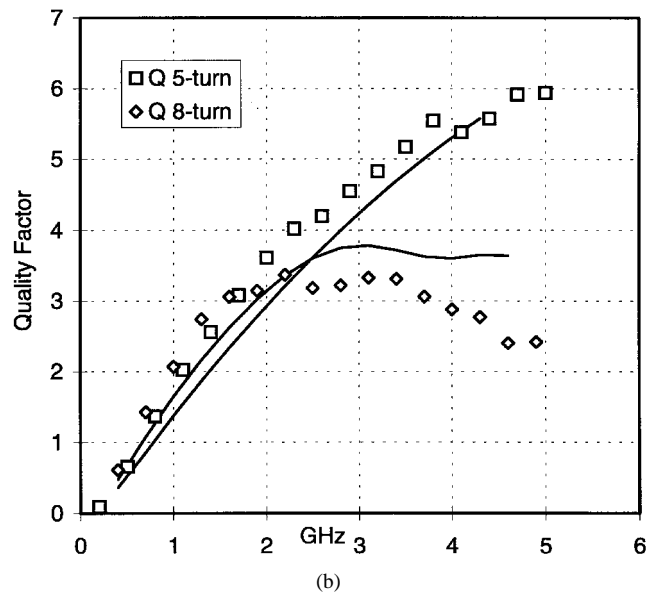
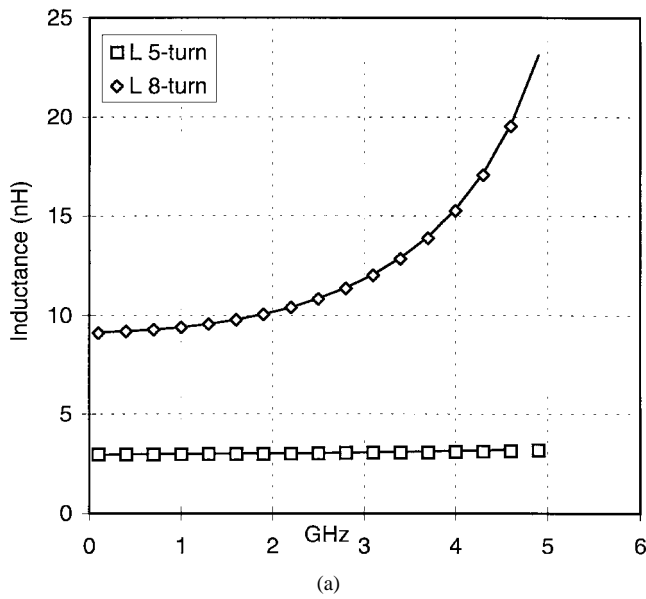


Fig. 10. (a) Extracted inductance of square spirals from measurements and simulations. (b) Extracted Q -factor of square spirals from measurements and simulations.

is a decreasing function of frequency. In the frequency range of interest, the Q is a combination of the above-mentioned effects and the Q peaks at some frequency f_{QMAX} . Notice that our analysis predicts this frequency well. This is important since we can design inductors that have peak Q at the frequency of interest.

We model the inductors using the equivalent circuits of Fig. 6(b). Table II compares our results, including the total error involved in the modeling. The error is derived by computing the relative error between the two-port measured s -parameters and the model two-port s -parameters. The error is cumulative over 16 points in the frequency range. Two models were generated, one based on the actual measurement results and the other based solely on simulation results (the simulation model is not a curve-fitted model of the measurements but rather a curve fit to the simulations).

TABLE II
SIMULATED AND MEASURED MODELS OF SQUARE SPIRALS

Model Parameter	Meas 5-turn	Sim 5-turn	Meas 8-turn	Sim 8-turn
L (nH)	2.93	2.97	8.78	8.55
R (Ω)	8.02	8.23	17.50	16.99
C_{sl} (fF)	93.5	174.4	176.9	152.6
C_{sj} (fF)	210.7	341.8	656.6	179.9
R_{sj} (Ω)	1.35k	377	527.6	290.2
R_{s2} (Ω)	1.06k	472	587.0	314.7
C_{BR} (fF)	22.4	88.9	63.4	106.2
Σ error ²	.06	0.30	0.37	0.52

TABLE III
POLYGON SPIRAL GEOMETRY

Spirals	L4	L6	L7	L8	L9	L11
Radius R (μm)	105	105	105	105	105	105
Width W (μm)	8.2	7.5	7.5	7.5	7.5	6.5
Space S (μm)	3	3	3	3	3	3
Turns N	6.75	8	8	8	8	7.75
No. of sides	12	12	12	12	12	12
Metal (s)	M2	M2	1+2 via ⁽⁺⁾	1+2 via ⁽⁻⁾	1+2+3	M2

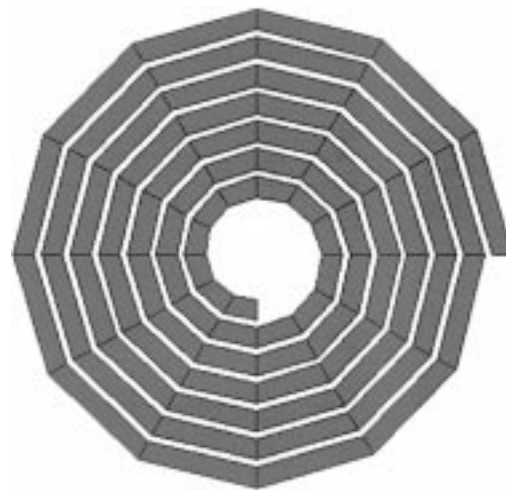


Fig. 11. Layout of polygon spiral inductor L4.

D. Polygon Spiral Inductors

Since polygon spirals with more than four sides have higher Q than square spirals (for the same area), it is advantageous to use these structures. Many spirals are measured and compared with simulation. The geometry of the fabricated spirals is shown in Table III. The chip layout of a sample spiral inductor L4 appears in Fig. 11. S -parameters are plotted for the L4 spiral in Fig. 12, and again good agreement is found between simulation and measurement. Extracted series inductance and Q for the L4 and L11 spirals are plotted in Fig. 13(a) and (b). The inductors are also modeled using the equivalent circuit of Fig. 6(b), and Table IV summarizes the model parameters based on measurement and simulation.

E. Multimetal Spiral Inductors

To improve the low-frequency Q of the spiral, we can place metal layers in shunt to reduce the series resistance of the

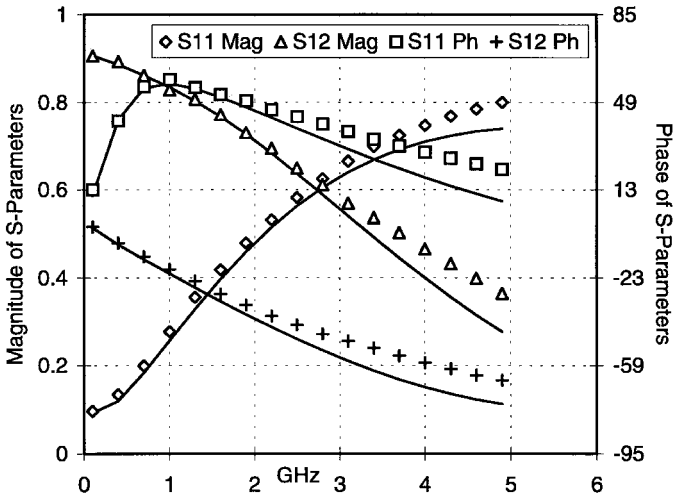
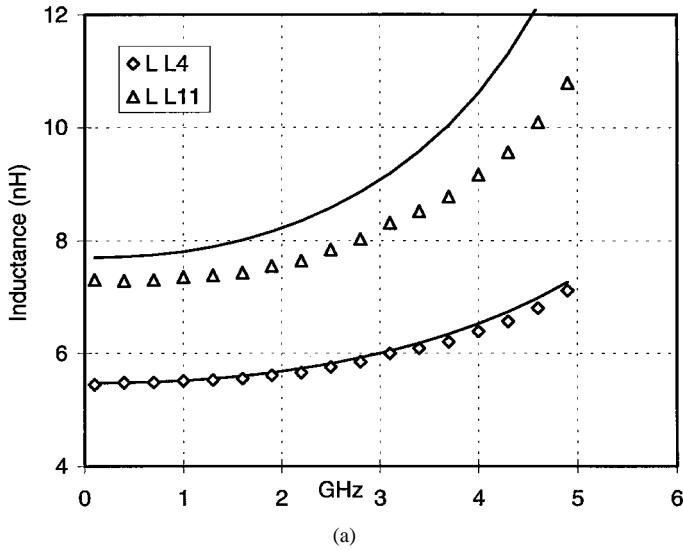
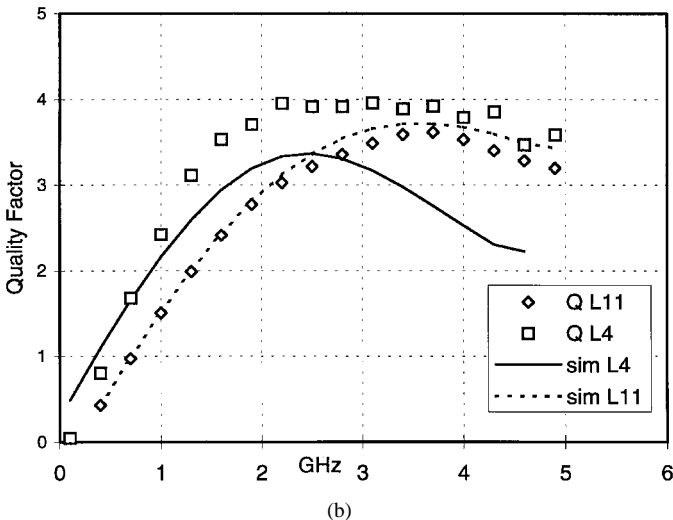


Fig. 12. Measured and simulated *s*-parameters of the L4 polygon spiral.



(a)



(b)

Fig. 13. (a) Extracted inductance of polygon spirals from measurement and simulation. (b) Extracted *Q*-factor of polygon spirals from measurement and simulation.

TABLE IV
SIMULATED AND MEASURED MODELS OF POLYGON SPIRALS

Model Parameter	Meas L4	Sim L4	Meas L11	Sim L11
<i>L</i> (nH)	5.45	5.67	7.3	7.7
<i>R</i> (Ω)	10.3	11.5	16.0	16.4
<i>C_{sl}</i> (fF)	132	225	134	208
<i>C_{sl}</i> (fF)	336	280	320	258
<i>R_{sl}</i> (Ω)	765	711	762	832
<i>R_{s2}</i> (Ω)	726	723	769	869
<i>C_{BR}</i> (fF)	45	55	45	55
Σ error ²	0.02	0.20	0.07	0.24

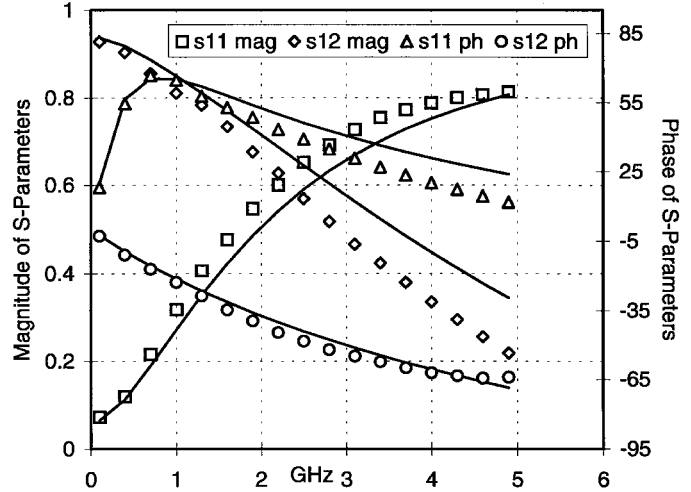


Fig. 14. Measured and simulated *s*-parameters of the M1–M2 multimetal polygon spiral L7.

spiral. To test this, the spiral L6 in the polygon set was used. Three new inductors L7–L9 were constructed. L7 has two L6 spirals on metal 2 and metal 1 connected in shunt with as many vias as possible; L8 also has two L6 spirals in shunt, but with vias placed only at the ends of the segments. Last, L9 has all metals connected in shunt (except where it was necessary to use metal 0 to connect to the inner turn of the spiral).

Simulations were run for the M2 + M1 spiral, and measured and simulated *s*-parameters are shown in Fig. 14. Good agreement is found as before. Fig. 15(a) plots the extracted series inductance of the spirals. Due to the tight coupling, the inductance value of the metal–metal structure does not drop much. Fig. 15(b) plots the extracted *Q* of the spirals. The low-frequency *Q* enhancement of the metal–metal structure is due to the drop in series resistance, in accordance with connecting the appropriate metal layers in shunt. At high frequency, though, the picture changes greatly due to substrate loss. At high frequency, the *Q* of the single metal layer is actually better.

Fig. 16 compares the measured *Q* of L6–L9. The measurement results indicate an overall *Q*-increase at low frequency for the M1 + M2 cases, but using three metal layers is actually harmful at all frequencies (since the M0 layer is very close to the substrate). Also, the *Q* of L8 is slightly higher than the *Q* of L7, demonstrating that use of ample vias helps to boost the *Q* in the shunt configuration.

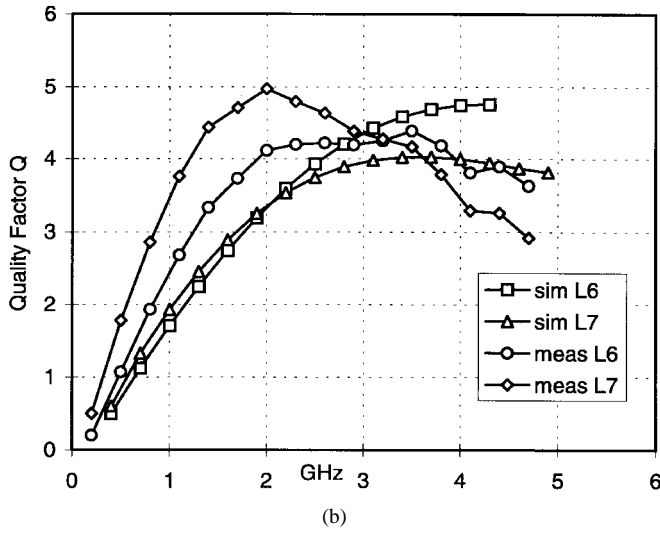
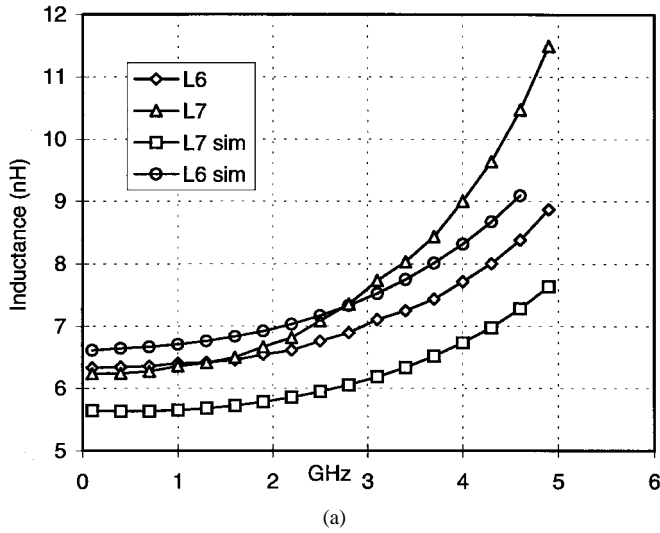


Fig. 15. (a) Extracted inductance of polygon spirals L6 and L7. (b) Extracted quality factor of polygon spirals L6 and L7.

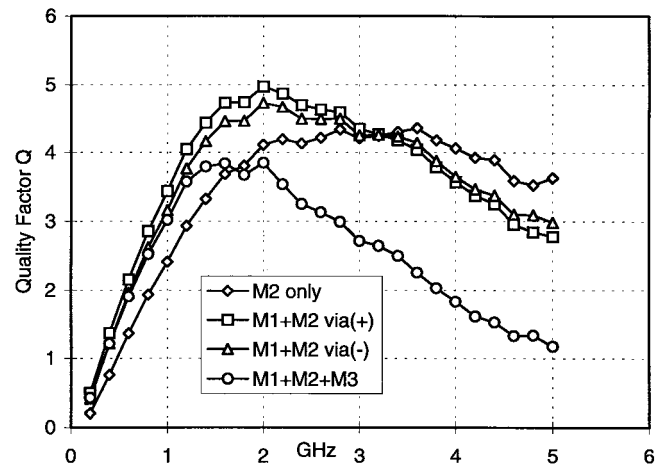


Fig. 16. Measured Q -factor enhancement of multimetal shunt connected spirals.

F. Coupled Spiral Inductors

Many RF IC designs incorporate several spiral inductors on the same die. Since these structures are physically large,

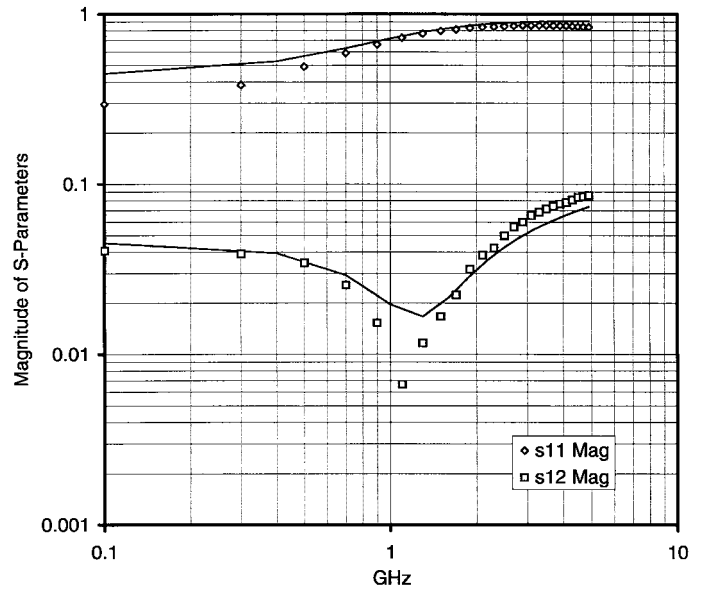


Fig. 17. Measured and simulated s -parameters of the coupled spirals.

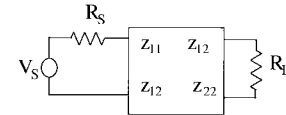


Fig. 18. Circuit for calculating the power delivered to a resistive load from a reciprocal two-port network.

substrate coupling can be a significant problem. For instance, in any amplification stage, the substrate coupling can act as parasitic feedback, lowering the gain and possibly causing oscillations to occur. Hence, it is very important to model the substrate coupling.

The s -parameters of two eight-turn square spirals separated by a distance of $100 \mu\text{m}$ were simulated and measured. Fig. 17 shows the magnitude of the measured and simulated s -parameters. As can be seen from the figure, simulation results predict the coupling behavior accurately, such as the minimum S_{21} . To gain further insights into the coupling, we plot the power isolation from one spiral to the other using the following equations. For the arbitrary passive two-port shown in Fig. 18, the ratio of the power delivered to a resistive load R_L through the two-port can be shown to be

$$\frac{P_L}{P_{in}} = \frac{R_L \| G_I \|^2}{\text{Re}[Z_{in}]} \tag{22}$$

In the above equation, G_I is the current gain through the two-port and Z_{in} is the impedance looking into the two-port from the source side

$$G_I = \frac{z_{12}}{R_L + z_{12}} \tag{23}$$

$$Z_{in} = z_{11} - \frac{z_{12}^2}{R_L + z_{22}} \tag{24}$$

Using the above equations, we plot the measured and simulated power isolation for the coupled inductors in Fig. 19, where a $50\text{-}\Omega$ load resistance is used in the above equations. Clearly, there are two frequencies where the isolation is

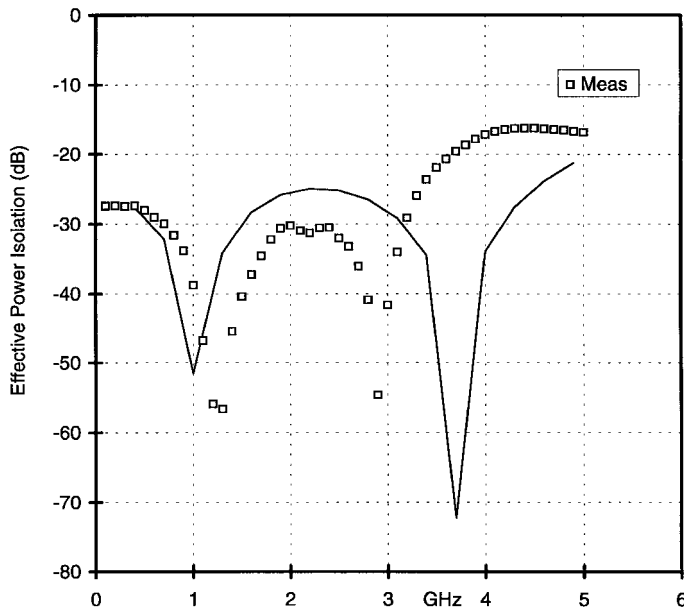


Fig. 19. Measured and simulated isolation between the coupled spirals.

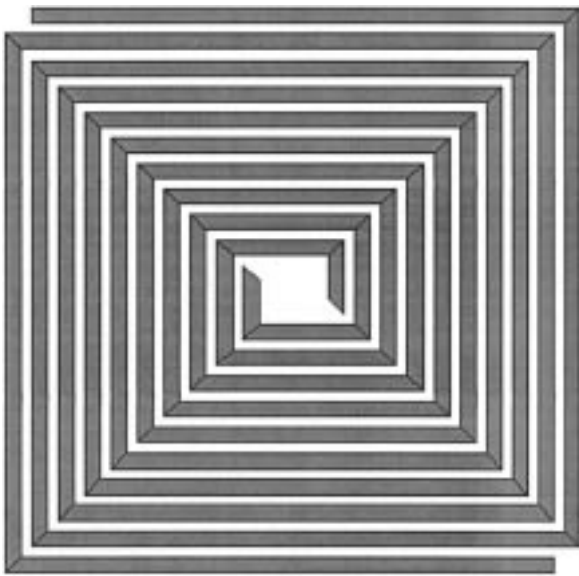


Fig. 20. Layout of planar transformer.

maximum. These frequencies depend on the geometrical layout of the spirals, and this gives the designer the powerful option of placing the spirals in locations to maximize isolation.

G. Planar Transformers

To test the simulation accuracy for transformers, several planar transformers were fabricated and measured. An example transformer structure is shown in Fig. 20. The transformer is made of two interwound spirals each of five turns of $7\text{-}\mu\text{m}$ -wide metal with a spacing of $17\ \mu\text{m}$. Measured and simulated s -parameters are shown in Fig. 21. Again, good agreement is found between simulation and measurement. We can gain further insight into the measurement results by using (22) to plot the measured loss of the transformer as a function of load

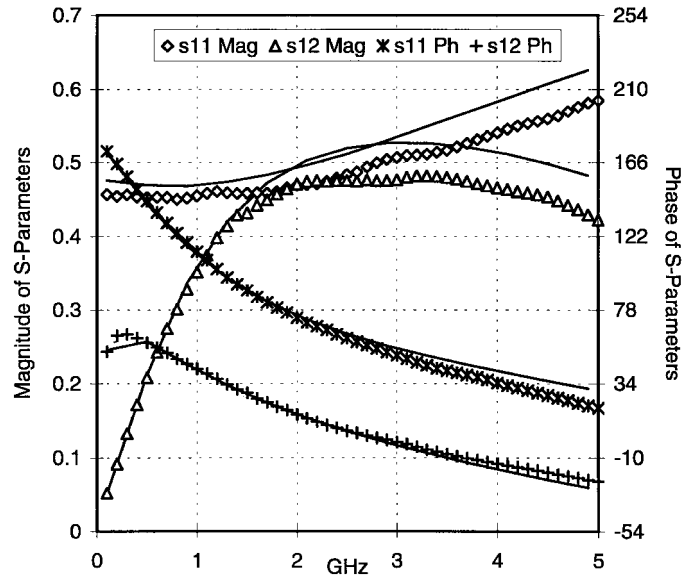


Fig. 21. Measured and simulated s -parameters of planar transformer.

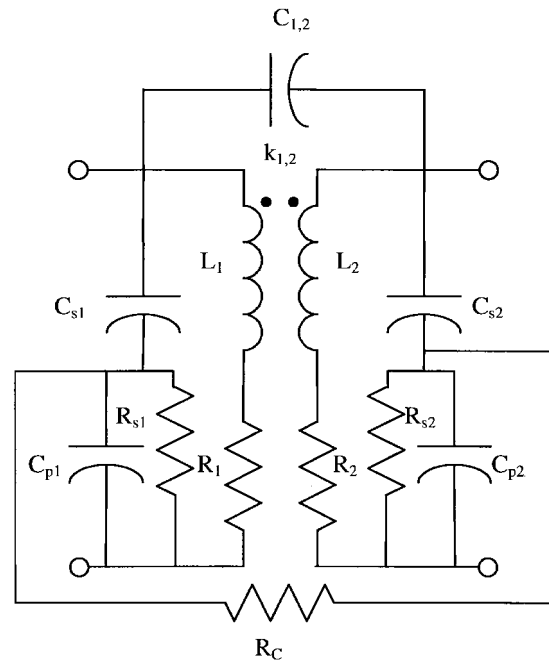


Fig. 22. Equivalent circuit model for planar transformer.

resistance. One can find the optimal value of load resistance at the frequency of interest to minimize losses.

The dynamics of the transformer can be captured in a compact model similar to the coupled inductors, as shown in Fig. 22. The k factor for planar inductors is about 0.7–0.8. Substrate coupling is again modeled with R_C . While the circuit of Fig. 22 is physically based, one can also derive the equivalent circuit, which contains an ideal transformer at the core with parasitic elements [7], [19]. The model parameters from measurement and simulation appear in Table V.

V. CONCLUSION

In this paper, we presented techniques to analyze, model, and optimize spiral inductors and transformers on the Si

TABLE V
SIMULATED AND MEASURED MODELS OF PLANAR TRANSFORMER

Transformer Model Parameter	Measured	Simulated
L (nH)	4.88	4.63
R (Ω)	17.58	16.91
C_s (fF)	124	123
C_p (fF)	430	418
R_s (Ω)	243	252
R_C (Ω)	1.00k	796
$C_{1,2}$ (fF)	53	59
$k_{1,2}$.703	0.715
$\Sigma \text{ error}^2$	0.79	0.04

substrate. The techniques are accurate, taking into account substrate coupling, current constriction, and proximity effects. The analysis is also fast and efficient, making it suitable for computer optimization. Furthermore, the analysis is general and appropriate for analyzing any arbitrary arrangement of conductors, such as multimetal spirals. A custom CAD tool called ASITIC was developed that incorporates the algorithms discussed in this paper. ASITIC was used to analyze a wide variety of test structures such as square spirals, polygon spirals, coupled spirals, and transformers. The test spirals were also fabricated, and measurement results compared well to simulation. Compact models for the various devices were presented that model the device dynamics over a wide frequency range.

ACKNOWLEDGMENT

The authors thank W. Mack, J. Eisenstadt, and Y. Nguyen of Philips Semiconductors for their help and support in fabricating and measuring the spirals. Also, the authors thank R. Gharpurey of Texas Instruments for his valuable insights.

REFERENCES

- [1] N. M. Nguyen and R. G. Meyer, "Si IC-compatible inductors and LC passive filters," *IEEE J. Solid-State Circuits*, vol. 27, pp. 1028–1031, Aug. 1990.
- [2] K. B. Ashby, W. C. Finley, J. J. Bastek, S. Moinian, and I. A. Koullias, "High Q inductors for wireless applications in a complementary silicon bipolar process," in *Proc. Bipolar and BiCMOS Circuits and Technology Meeting*, Minneapolis, MN, 1994, pp. 179–182.
- [3] J. N. Burghartz, M. Soyuer, and K. Jenkins, "Microwave inductors and capacitors in standard multilevel interconnect silicon technology," *IEEE Trans. Microwave Theory Tech.*, vol. 44, pp. 100–103, Jan. 1996.
- [4] R. B. Merrill, T. W. Lee, H. You, R. Rasmussen, and L. A. Moberly, "Optimization of high Q integrated inductors for multi-level metal CMOS," *IEDM*, 1995, pp. 38.7.1–38.7.3.
- [5] L. Zu, Y. Lu, R. C. Frye, M. Y. Law, S. Chen, D. Kossiva, J. Lin, and K. L. Tai, "High Q -factor inductors integrated on MCM Si substrates," *IEEE Trans. Comp., Packag., Manufact. Technol. B*, vol. 19, pp. 635–643, Aug. 1996.
- [6] J. Y.-C. Chang and A. A. Abidi, "Large suspended inductors on silicon and their use in a 2- μm CMOS RF amplifier," *IEEE Electron Device Lett.*, vol. 14, pp. 246–248, 1993.
- [7] J. R. Long and M. A. Copeland, "The modeling, characterization, and design of monolithic inductors for silicon RF IC's," *IEEE J. Solid-State Circuits*, vol. 32, pp. 357–369, Mar. 1997.
- [8] J. Craninckx and M. Steyaert, "A 1.8-GHz low-phase-noise CMOS VCO using optimized hollow spiral inductors," *IEEE J. Solid-State Circuits*, vol. 32, pp. 736–745, May 1997.
- [9] D. Lovelace and N. Camilleri, "Silicon MMIC inductor modeling for high volume, low cost applications," *Microwave J.*, Aug. 1994, pp. 60–71.

- [10] S. Ramo, J. R. Whinnery, and T. Van Duzer, *Fields and Waves In Communication Electronics*, 3rd ed. New York: Wiley, 1994, pp. 324–330.
- [11] A. Niknejad, R. Gharpurey, and R. G. Meyer, "Numerically stable green function for modeling and analysis of substrate coupling in integrated circuits," *IEEE Trans. Computer-Aided Design*, vol. 17, pp. 305–315, Apr. 1998.
- [12] A. E. Ruehli and H. Heeb, "Circuit models for three-dimensional geometries including dielectrics," *IEEE Trans. Microwave Theory Tech.*, vol. 40, pp. 1507–1516, July 1992.
- [13] F. W. Grover, *Inductance Calculations*. Princeton, NJ: Van Nostrand, 1946 (also New York: Dover, 1954).
- [14] W. T. Weeks, L. L. Wu, M. F. McAllister, and A. Singh, "Resistive and inductive skin effect in rectangular conductors," *IBM J. Res. Develop.*, vol. 23, pp. 652–660, Nov. 1979.
- [15] R. Gharpurey, private communication.
- [16] C. P. Yue and S. S. Wong, "On-chip spiral inductors with patterned ground shields for Si-based RF IC's," in *Symp. VLSI Circuits Dig.*, June 1997, pp. 85–86.
- [17] C. P. Yue, C. Ryu, J. Lau, T. H. Lee, and S. S. Wong, "A physical model for planar spiral inductors on silicon," in *Int. Electron Devices Meeting Tech. Dig.*, Dec. 1996, pp. 155–158.
- [18] R. Groves, K. Stein, D. Harame, and D. Judas, "Temperature dependence of Q in spiral inductors fabricated in a silicon-germanium/BiCMOS technology," in *Proc. 1996 Bipolar/BiCMOS Circuits and Technology Meeting*, New York, 1996, pp. 153–156.
- [19] D. O. Pederson and K. Mayaram, *Analog Integrated Circuits for Communications*. Norwell, MA: Kluwer, 1991, pp. 183–184.



Ali M. Niknejad (S'92) was born in Tehran, Iran, on July 29, 1972. He received the B.S.E.E. degree from the University of California, Los Angeles, in 1994 and the master's degree in electrical engineering from the University of California, Berkeley, in 1997, where he is now pursuing the Ph.D. degree.

Mr. Niknejad has held several internship positions in the electronics industry. In the summer of 1994, he was with the Hughes Aircraft Advanced Circuit Technology Center, Torrance, CA, investigating wide-band current feedback op-amp topologies. During the summer of 1996, he was with Texas Instruments, Dallas, TX, where he studied substrate coupling. During the summer of 1997, he was with Lucent Technologies (Bell Labs), Murray Hill, NJ, where he investigated power amplifier topologies for wireless applications. His current research interests include high-frequency electronic circuit design, modeling of passive devices and substrates coupling, digital wireless communication systems, numerical methods in electromagnetics, and radio-frequency computer-aided design.



Robert G. Meyer (S'64–M'68–SM'74–F'81) was born in Melbourne, Australia, on July 21, 1942. He received the B.E., M.Eng.Sci., and Ph.D. degrees in electrical engineering from the University of Melbourne in 1963, 1965, and 1968, respectively.

In 1968, he was an Assistant Lecturer in electrical engineering at the University of Melbourne. Since 1968, he has been with in the Department of Electrical Engineering and Computer Sciences, University of California, Berkeley, where he is now a Professor. His current research interests are high-frequency analog integrated-circuit design and device fabrication. He has been a Consultant on electronic circuit design for numerous companies in the electronics industry. He is a coauthor of the book *Analysis and Design of Analog Integrated Circuits*, (New York: Wiley, 1993), and is editor of the book, *Integrated Circuit Operational Amplifiers* (New York: IEEE Press, 1978).

Dr. Meyer was President of the IEEE Solid-State Circuits Council. He was an Associate Editor of the IEEE JOURNAL OF SOLID-STATE CIRCUITS and IEEE TRANSACTIONS ON CIRCUITS AND SYSTEMS.